








EDGE: a new model for nuclear star cluster formation in dwarf galaxies

Emily I. Gray ¹★, Justin I. Read ¹, Ethan Taylor,¹ Matthew D. A. Orkney ^{2,3}, Martin P. Rey ⁴, Robert M. Yates ⁵, Stacy Y. Kim,⁶ Noelia E. D. Noël,¹ Oscar Agertz ⁷, Eric P. Andersson ⁸ and Andrew Pontzen⁹

¹Department of Physics, University of Surrey, Guildford Surrey, GU2 7XH, UK

²Institut de Ciències del Cosmos (ICCUB), Universitat de Barcelona, Martí Franquès 1, E-08028 Barcelona, Spain

³Institut d'Estudis Espacials de Catalunya (IEEC), E-08034 Barcelona, Spain

⁴Sub-Department of Astrophysics, University of Oxford, DWB, Keble Road, Oxford OX1 3RH, UK

⁵Centre for Astrophysics Research, University of Hertfordshire, Hatfield AL10 9AB, UK

⁶Carnegie Theoretical Astrophysics Center, Carnegie Observatories, 813 Santa Barbara Street, Pasadena, CA 91101, USA

⁷Lund Observatory, Division of Astrophysics, Department of Physics, Lund University, Box 43, SE-221 00 Lund, Sweden

⁸Department of Astrophysics, American Museum of Natural History, 200 Central Park West, New York, NY 10024-5102, USA

⁹Institute for Computational Cosmology, Department of Physics, Durham University, South Road, Durham DH1 3LE, UK

Accepted 2025 March 28. Received 2025 March 16; in original form 2024 May 30

ABSTRACT

Nuclear star clusters (NSCs) are among the densest stellar systems in the Universe and are found at the centres of many spiral and elliptical galaxies, and up to ~ 40 per cent of dwarf galaxies. However, their formation mechanisms, and possible links to globular clusters (GCs), remain debated. This paper uses cosmological simulations of dwarf galaxies at a spatial resolution of ~ 3 pc to present a new formation mechanism for NSCs, showing they naturally emerge in a subset dwarfs with present-day halo masses of $\sim 5 \times 10^9 M_{\odot}$. The mechanism proceeds following reionization quenching that stops the supply of cold star-forming gas. Next, a major merger causes a central dense gas reservoir to form, eventually exciting rapid cooling, leading to a significant starburst. An NSC forms in this starburst that quenches star formation thereafter. The result is a nucleated dwarf that has two stellar populations with distinct age: pre- and post-reionization. Our mechanism is unique because of the low mass of the host dwarf, and because it naturally leads to NSCs that contain two stellar populations with a $\gtrsim 1$ billion year age separation. The former means that NSCs, formed in this way, can accrete on to galaxies of almost all masses. If these accreted NSCs fall to the centre of their host galaxy, they could then seed the formation of NSCs everywhere. The latter yields a predicted colour–magnitude diagram that has two distinct main sequence turn-offs. Several GCs orbiting the Milky Way, including Omega Centauri and M54, show similar behaviour, suggesting that they may be accreted NSCs.

Key words: methods: numerical – galaxies: dwarf – galaxies: evolution – galaxies: haloes – galaxies: star clusters: general – dark matter.

1 INTRODUCTION

Nuclear star clusters (NSCs) are dense stellar systems with stellar masses and half-light radii in the range $M_{\star} \sim 10^{5-8} M_{\odot}$ and $r_{1/2} \sim 1-30$ pc, respectively (see Neumayer, Seth & Böker 2020 for a review). They are most common within the centres of intermediate-mass galaxies (~ 90 per cent of $M_{\star} \sim 10^{9.5} M_{\odot}$ galaxies) but are also found in up to ~ 40 per cent of dwarf galaxies [DGs; defined here as galaxies with stellar mass $M_{\star} < 10^9 M_{\odot}$ (Collins & Read 2022)], with an occupation fraction that decreases with the mass of the host galaxy (Sánchez-Janssen et al. 2019; Hoyer et al. 2021; Carlsten et al. 2022). The common co-existence of these clusters with supermassive black holes (SMBHs) suggests that they could be promising sites for the formation of SMBH seeds (e.g. Ferrarese et al. 2006). And, through the mergers of stellar remnants, they are also crucibles for the

formation of gravitational waves (e.g. Antonini, Gieles & Gualandris 2019).

Despite their ubiquity, the formation channels of NSCs remain uncertain. One key proposal is that NSCs in low-mass galaxies form from the in-fall and mergers of globular clusters (GCs; Tremaine, Ostriker & Spitzer 1975). This is motivated by the observed similarities between massive GCs and NSCs [specifically, their stellar mass and luminosity (McLaughlin 1999; Côté et al. 2006; Den Brok et al. 2014)]. More massive GCs also have more rapid dynamical friction time-scales, and this injection of less-enriched stars into galactic centres may provide an explanation for the origin of metal-poor nuclei that are common in low-mass galaxies (e.g. Spengler et al. 2017). This formation scenario is further supported by observations of early-type galaxies that show a lack of GCs within their inner regions, implying that these have fallen into the centre (Lotz et al. 2001; Capuzzo-Dolcetta & Mastrobuono-Battisti 2009). Additionally, there is a proven correlation between the frequency of

* E-mail: eg00451@surrey.ac.uk

nucleated early-type galaxies and GCs (Miller & Lotz 2007; Lim et al. 2018; Sánchez-Janssen et al. 2019).

However, GC mergers alone are not sufficient to explain the late-time star formation observed in the NSCs of more massive galaxies ($M_* \gtrsim 10^9 M_\odot$; Seth et al. 2006, 2008a; Walcher et al. 2006; Kacharov et al. 2018; Fahrion et al. 2022b), including the Milky Way (Paumard et al. 2006; Lu et al. 2008; Feldmeier-Krause et al. 2015; Nguyen et al. 2019) and M31 (Bender et al. 2005; Georgiev & Böker 2014; Carson et al. 2015). For these NSCs at least, some mechanisms for further gas accretion and star formation is required. Proposals include gas accretion and cooling in major mergers (Mihos & Hernquist 1994; Milosavljević 2004; Hopkins & Quataert 2010; Guillard, Emsellem & Renaud 2016; Brown, Gnedin & Li 2018), gas accretion along a non-axisymmetric stellar bar (Shlosman, Begelman & Frank 1990), tidal forces causing gas compression (Emsellem & Van De Ven 2008), and/or clumpy star formation at high redshifts (Bekki, Couch & Shioya 2006; Bekki 2007). The need for late-time star formation in these NSCs is further supported by N -body simulations of GC mergers (Capuzzo-Dolcetta & Mocchi 2008). These are able to explain some features of NSCs, such as their mass and size, but cannot account for their observed rotation that also implies at least some dissipation and *in situ* star formation (Seth et al. 2006, 2008b; Hartmann et al. 2011; Carson et al. 2015; Tsatsi et al. 2017; Nguyen et al. 2019).

It is likely that some mix of gas accretion and GC mergers is required to reproduce the full population statistics of NSCs, as is supported by semi-analytic models (e.g. Gnedin, Ostriker & Tremaine 2014; Antonini, Barausse & Silk 2015), and recent high-resolution N -body hydrodynamical simulations (van Donkelaar et al. 2024). The mass of the host galaxy likely dictates which of these mechanisms are dominant in each case, such that lower mass galaxies favour GC in-fall, whereas galaxies with $M_* > 10^9 M_\odot$ are better explained by the *in situ* star formation scenario (Neumayer et al. 2020; Fahrion et al. 2021, 2022a, b). However, it remains an open question where the GCs come from in the first place.

Previous simulations in the literature have studied NSC formation in DGs. Guillard et al. (2016) use hydrodynamical simulations of isolated gas-rich dwarfs to introduce a ‘wet migration’ formation scenario. The LYRA simulations (Gutcke et al. 2022b) are cosmological simulations of low-mass dwarfs ($M_{200} \sim 10^9\text{--}10 M_\odot$) at a mass resolution of $M_{\text{baryon}} = 4 M_\odot$ and $M_{\text{DM}} = 80 M_\odot$. They report the presence of an NSC in one of their low-mass dwarfs, but do not directly address NSC formation mechanisms (Gutcke et al. 2022a).

In this paper, we use simulations of a $M_{200c} \sim 5 \times 10^9 M_\odot^1$ DG, drawn from the ‘Engineering Dwarfs at Galaxy formation’s Edge’ (EDGE²) project, to present a new mechanism for the formation of NSCs. These dwarfs are more massive than those previously studied in EDGE, reaching a post-reionization mass that has previously been found to stimulate renewed star formation (Rey et al. 2020). We find that, at this mass scale, a new phenomenon can occur: self-quenching by stellar feedback following a major-merger-driven starburst. The formation of an NSC is a natural result of this starburst. To fully understand this new NSC formation mechanism, we consider three ‘genetically modified’ versions of the same galaxy, engineered to have the major merger earlier and later. We also resimulate the same galaxy with a different random number seed to study the impact

of stochasticity (that impacts both when stars form, and when they explode) on the starburst and the final galaxy properties. We show that in all cases, except where the host galaxy is not fully quenched by reionization, an NSC forms with two distinct stellar populations with distinct ages. We explore the observational properties of our simulated NSCs, including their luminosity, size, chemistry, and kinematics, and we discuss how these predictions compare to the latest data for nearby NSCs and GCs.

This paper is organized as follows. In Section 2, we describe the EDGE suite and the specific simulations that we study in this work. In Section 3, we present the results from our simulations including the emergence of NSCs in EDGE, how they form, and their observational properties. In Section 4, we discuss the broader implications of these findings for both GC and NSC formation. Finally, in Section 5 we present our conclusions.

2 METHOD

We study an isolated DG of virial mass $M_{200c} = 5.79 \times 10^9 M_\odot$ at redshift $z = 0$, drawn from a suite of cosmological high-resolution zoom simulations: EDGE (introduced in Agertz et al. 2020). All of the EDGE simulations presented here are run until $z = 0$ assuming a Lambda cold dark matter cosmology with cosmological parameters as determined by the Planck satellite mission: $\Omega_m = 0.309$, $\Omega_\Lambda = 0.691$, $\Omega_b = 0.045$, and $H_0 = 67.77 \text{ km s}^{-1} \text{ Mpc}^{-1}$ (Planck Collaboration XVI 2014).

EDGE utilizes the adaptive mesh refinement hydrodynamics code, RAMSES (Teyssier 2002), to track the evolution of stars, dark matter, and gas. We have a maximum spatial resolution of 3 pc and a mass resolution of $M_{\text{gas}} = 161 M_\odot$, $M_* = 300 M_\odot$, and $M_{\text{DM}} = 945 M_\odot$ for the fiducial simulations. The galaxy formation model implements star formation, stellar feedback, cosmic reionization, and gas cooling and heating. Cosmic reionization is modelled as a time-dependent source of heating spread uniformly across our simulation box (Haardt & Madau 1995; Rey et al. 2020).

We adopt the following star formation relation, shown in equation (1) (Schmidt 1959; Kennicutt 1998):

$$\dot{\rho}_* = \varepsilon_{\text{ff}} \frac{\rho_g}{t_{\text{ff}}} \text{ for } \rho_g > \rho_{\text{SF}} \text{ and } T_g < T_{\text{SF}}, \quad (1)$$

where $\dot{\rho}_*$ is the star formation rate (SFR), ε_{ff} is the star formation efficiency per free-fall time, ρ_g is the gas density in the cell, t_{ff} is the local gas free-fall time, ρ_{SF} is the density threshold for star formation, T_g is the gas temperature in the cell, and T_{SF} is the maximum allowed temperature for star formation. ρ_{SF} and T_{SF} are set to $300 \text{ m}_H \text{ cm}^{-3}$ and 100 K, respectively. t_{ff} is calculated as $\sqrt{3\pi/32G\rho}$ and ε_{ff} is fixed to 10 per cent, as per Gridale et al. (2019). For each cell that satisfies the star formation criteria, equation (1) is used along with the cell volume and time-step to calculate the probability of forming stars (e.g. Rasera & Teyssier 2006; Dubois & Teyssier 2008). Poisson sampling is then used to find the number of star particles of discrete $300 M_\odot$ masses (see Agertz et al. 2013 for a detailed explanation of the procedure we adopt).

Due to the high spatial and mass resolution of the EDGE simulations, we can track the impact of individual supernovae on their surrounding interstellar medium accurately (Kimm et al. 2015), without the need for delayed cooling (e.g. Stinson et al. 2006), additional momentum injection, or similar (Read, Agertz & Collins 2016; Agertz et al. 2020). At each time-step, if a star’s mass is above $8 M_\odot$, it has a probability of undergoing core-collapse due to the random sampling of equation (6) in Agertz et al. (2013). This ensures a continuous but discrete injection of energy, momentum, and metals

¹ M_{200c} is the mass within the virial radius (r_{200c}), which is defined as the radius at which the mean enclosed density of the dwarf equals $200 \times$ the critical density of the Universe.

²<https://edge-simulation.github.io/>

Table 1. Key information about the EDGE-simulated dwarfs and their NSCs, including the half-light radius from the Sérsic fits (see Fig. 1), the virial radius (of the dwarf), masses, and the average [Fe/H] and [O/Fe]. For the dwarfs, the masses and metallicities are within the virial radius, whereas for the NSCs these are within the 4 half-light radius. The v -band magnitude within four times the half-light radius is added for the NSCs. The redshift the major merger occurs and its total mass ratio in comparison to the main halo is recorded.

Dwarf	$r_{1/2}$ (pc)	r_{200} (pc)	$M_{\text{tot}} (<r_{200})$ (M_{\odot})	$M_{\star} (<r_{200})$ (M_{\odot})	$M_{\text{gas}} (<r_{200})$ (M_{\odot})	[Fe/H] (dex)	[O/Fe] (dex)	Merger redshift	Merger ratio
Reference	365.4 ± 4.4	3.8×10^4	5.8×10^9	3.2×10^6	3.0×10^7	-2.0 ± 0.4	0.6 ± 0.2	2.33	0.93
Diff. Seed	127.0 ± 2.4	3.7×10^4	5.6×10^9	9.6×10^6	5.1×10^5	-1.8 ± 0.3	0.5 ± 0.2	2.33	0.91
Later	75.8 ± 1.3	3.7×10^4	5.3×10^9	3.3×10^6	2.0×10^7	-2.0 ± 0.5	0.7 ± 0.1	1.27	0.36
Earlier	331.8 ± 8.8	3.8×10^4	5.7×10^9	4.4×10^6	5.5×10^7	-2.0 ± 0.6	0.5 ± 0.3	3.35	0.62
NSC	$r_{1/2}$ (pc)		$M_{\text{tot}} (<4r_{1/2})$ (M_{\odot})	$M_{\star} (<4r_{1/2})$ (M_{\odot})	$M_{\text{gas}} (<4r_{1/2})$ (M_{\odot})	[Fe/H] (dex)	[O/Fe] (dex)		$M_v (<4r_{1/2})$ (mag)
Reference	9.9 ± 1.3		3.1×10^5	2.8×10^5	5.2	-1.9 ± 0.1	0.5 ± 0.1		-8.06
Diff. Seed	9.8 ± 0.2		1.4×10^6	1.3×10^6	50	-1.9 ± 0.1	0.4 ± 0.1		-9.64
Later	4.4 ± 0.8		7.7×10^5	6.9×10^5	53	-2.0 ± 0.5	0.6 ± 0.1		-9.23

from supernova, as described in Agertz et al. (2013) and Agertz et al. (2020). Energy from supernovae is injected purely thermally, if the cooling radius is well resolved (> 90 per cent of the time). If not, some additional momentum is also injected to compensate for overcooling (see Agertz et al. 2020). Alongside supernovae, we account for stellar winds from massive stars ($\gtrsim 5 M_{\odot}$) through continuous injection. We do not explicitly model radiative transfer (photoionization or photoheating) from young stars. For a more in-depth description of the physics and sub-grid model employed in the EDGE simulations, see Rey et al. (2019), Agertz et al. (2020), Rey et al. (2020), and Orkney et al. (2021).

The GENETIC software (Stopyra et al. 2021) provides the initial conditions for these galaxies while also implementing a genetic modification framework that allows us to investigate different mass accretion histories for each galaxy within cosmic variance (Roth, Pontzen & Peiris 2016; Rey & Pontzen 2018). We change the density peak of the main halo progenitor at redshift $z = 4$, but ensure the mean density of the associated Lagrangian region is kept constant. This allows us to modify the halo mass at around reionization while keeping halo mass at redshift $z = 0$ fixed.

Halo selection is done using the HOP halo finder (Eisenstein & Hut 1998) from a ‘void’ simulation (a 512^3 resolution dark-matter-only simulation that covers a 50 Mpc^3 patch of the universe) to be simulated at a higher resolution (Katz & White 1993; Oñorbe et al. 2014; Agertz et al. 2020). To ensure selected haloes are isolated, the virial radius (r_{200}) is used to find pairwise distances. Halo data are read and analysed using a combination of the PYNBODY (Pontzen et al. 2013) and TANGOS (Pontzen & Tremmel 2018) packages.

The four simulated dwarfs utilized in the paper are described in Table 1. Our initial unmodified simulated dwarf is referred to as ‘Reference’.³ We engineered this dwarf to begin forming later and earlier using the genetic modification framework. ‘Later’ refers to the dwarf that started its assembly history at a later epoch (overdensity of -20 per cent at $z=4$, and $+20$ per cent at $z=0$), whereas ‘Earlier’ refers to a dwarf that had longer to form before reionization (overdensity of $+30$ per cent at $z = 4$, and no modification at $z = 0$). Additionally, to study the effects of stochasticity, we rerun the unmodified simulation with the same initial conditions but a different random number seed (that impacts both when stars form and when they explode; see Section 2). This dwarf is referred to as ‘Different Seed’.

³Known as ‘Halo 383 Fiducial’ in the EDGE suite.

3 RESULTS

3.1 The emergence of NSCs in EDGE

Fig. 1 shows the surface brightness contours of the simulated dwarfs, providing an insight into the structure of the stellar population of the dwarfs and their NSCs at $z = 0$. The Reference, Different Seed, and Later simulations contain a dense nucleus (or NSC) – this is not seen for the Earlier simulation. The structural differences between the Reference and Different Seed simulations show how stochasticity impacts the size and stellar mass of our simulated NSCs. The NSC size is in good agreement between these runs but the stellar mass is different by a factor of 5, while the host galaxy size also differs by a factor of 3.

The cylindrically averaged radial surface brightness profiles of each simulation are shown in the bottom panels of Fig. 1 – the alignment of the dwarf does not affect the surface brightness profile. Two Sérsic profiles were fit to the nucleated dwarfs to provide an estimate for both the NSC and host galaxy half-light radii, with uncertainties. These values are given in Table 1. From here onwards, we define the NSC spatially as containing all stars within 4 NSC half-light radii, corresponding to the inflection in the surface brightness profiles (see Fig. 1). This double-Sérsic profile is typical of real DGs containing NSCs (Côté et al. 2006). A single Sérsic profile was fit to the non-nucleated Earlier simulation. The Later simulation has the smallest NSC radius and reaches the highest surface brightness. In this simulation, it is less clear at what radius we transition from the NSC to the host DG. This difficulty in separating the NSC from its host is also seen in some real nucleated dwarfs (Côté et al. 2007).

3.2 The formation of NSCs via a self-quenching starburst

In Fig. 2, we show graphically how an NSC forms in our Reference simulation. From top to bottom, the rows show images of stars, dark matter density, and gas density (in a 0.1 kpc thick slice along the z -direction) across multiple snapshots around the major merger event, which triggers the NSC-forming starburst. In the leftmost panels, the two proto-galaxies (the main halo and the major merger, a $\sim 1:1$ merger for this simulation, see Table 1) that will eventually form the final dwarf are shown. These experienced early star formation that was quenched by cosmic reionization and are not yet to a point where their star formation can reignite (see Rey et al. 2020, figs 3 and 4). As can be seen in the second column, ~ 2 billion years after reionization quenching, the main halo begins to merge with the companion of similar total mass. This causes a dense central gas reservoir to form

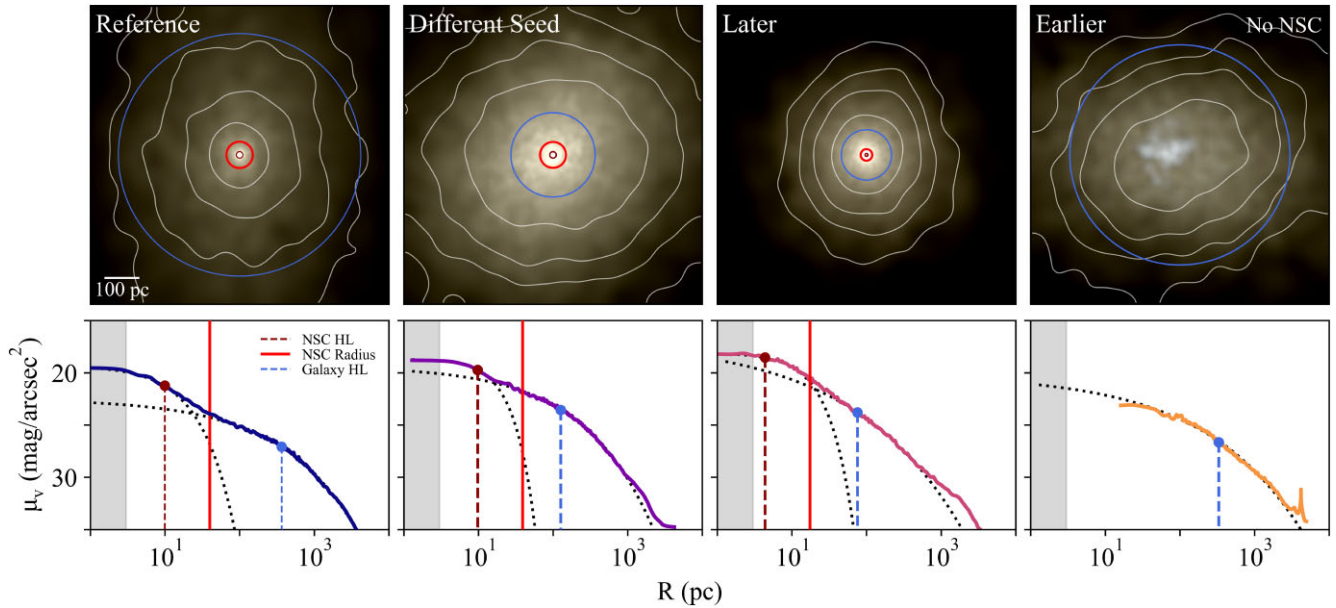


Figure 1. The emergence of NSCs in EDGE. Top: surface brightness contours (μ_v) overlay RGB images of the stars in our simulated dwarfs at redshift $z = 0$. A dense NSC is visible at the centres of the Reference, Different Seed, and Later simulations, but not the Earlier one. The images are aligned such that the angular momentum vector of the gas within 5 kpc corresponds to the z -axis that points towards the reader. Surface brightness contours are in the range 18–38 mag arcsec $^{-2}$. The RGB images span values in the range 23–28 mag arcsec $^{-2}$ in which the red, blue, and green channels are weighted by the I, V, and U bands, respectively. The blue, dark red, and red circles denote the total stellar population half-light radius, the NSC half-light radius, and the NSC radius, respectively. Bottom: surface brightness profiles of all the dwarfs at redshift $z = 0$. The black dotted curves show double Sérsic profile fits used to obtain the half-light radii. These are marked by the dark red dashed and blue dashed vertical lines, respectively (see also Table 1). The vertical red line denotes the NSC radii, which is 4 NSC half-light radii. The grey band to the left of each plot marks the simulation spatial resolution of 3 pc. Notice that the NSC is visible in the surface brightness profiles of Reference and Different seed as a high central surface brightness, with a point of inflection. For the Later simulation, the high central surface brightness still indicates the presence of an NSC, but the inflection is now less pronounced. The Earlier simulation has no NSC and its central surface brightness profile is lower than in the other simulations.

in the main halo, eventually exciting rapid cooling and a significant starburst. The NSC forms in this starburst from a mix of smooth and clumpy star formation, producing dense star clusters (middle panels) that eventually merge into the galaxy’s centre, joining the NSC (upper right panel). This starburst event is so sudden and strong that it exhausts all the remaining star-forming gas, self-quenching the galaxy.

3.2.1 The impact of assembly history and stochasticity

To help us understand our new NSC formation mechanism further, we study the effects of different assembly histories, and of stochasticity, using our full simulation suite. Fig. 3 shows the build-up of DM (top) and stellar (bottom) mass in each of our simulations. First, notice that the dark matter assembly histories for the Reference and Different Seed simulations almost perfectly overlap, as expected. But, they have different stellar mass growth curves (compare the blue and purple lines in the top and bottom panels). This difference in stellar mass occurs due to a different random number seed both when forming stars and when the most massive stars explode (see Section 2). The results are particularly sensitive for the second burst, driving a difference in the final stellar mass of a factor of ~ 3 just due to these stochastic effects (see Table 1). None the less, the formation of an NSC occurs in both cases.

Furthermore, the Reference and Earlier assembly histories lie within the 68 per cent confidence intervals of expected assembly trajectories: they are common (compare the blue and orange lines in Fig. 3 to the dark grey band). By contrast, the Later simulation lies outside the 95 per cent intervals and is therefore rarer. All of

the simulations were designed to reach the same final dark matter mass by $z = 0$ but have very different final stellar masses due to their distinct assembly histories, similar to what has been reported for lower mass EDGE dwarfs in Rey et al. (2019).

Fig. 4 shows how these different assembly histories impact the star formation histories for each of our simulations (top panel) and the HI gas mass (bottom panel). In all cases, there is a pre-reionization star formation. However, star formation in the Reference, Different Seed, and Later runs are sufficiently quenched by reionization. Their star formation only reignites again following a major merger after reionization (as marked by the crosses; for more information about these mergers, see Table 1). The bottom panel shows how gas builds up due to the major merger in each simulation. HI gas is able to build up in the main halo of each NSC forming case. However, only after this major merger is fully completed does the gas density reach high enough to excite cooling. This results in a significant NSC-forming starburst (with SFRs $> 10^{-2} M_{\odot} \text{yr}^{-1}$) shortly after the merger that then expels most of the gas, quenching star formation for the remainder of the simulation. The two resulting stellar populations forming at different epochs are subsequently referred to as the ‘pre-reionization’ and ‘starburst’ stars.

The major merger event for the Earlier simulation also causes an increase in gas mass and a more mild increase in the SFR. However, the gas build-up is less than in the other simulations, reaching a maximum HI gas mass of $\sim 5 \times 10^6 M_{\odot}$ in comparison to $> 10^7 M_{\odot}$ (see Fig. 4 bottom panel). To better understand the differences between the NSC-forming starburst in the Reference simulation and Earlier simulation in which no NSC forms, we now analyse the gas properties in each simulation in more detail. Fig. 5 shows images

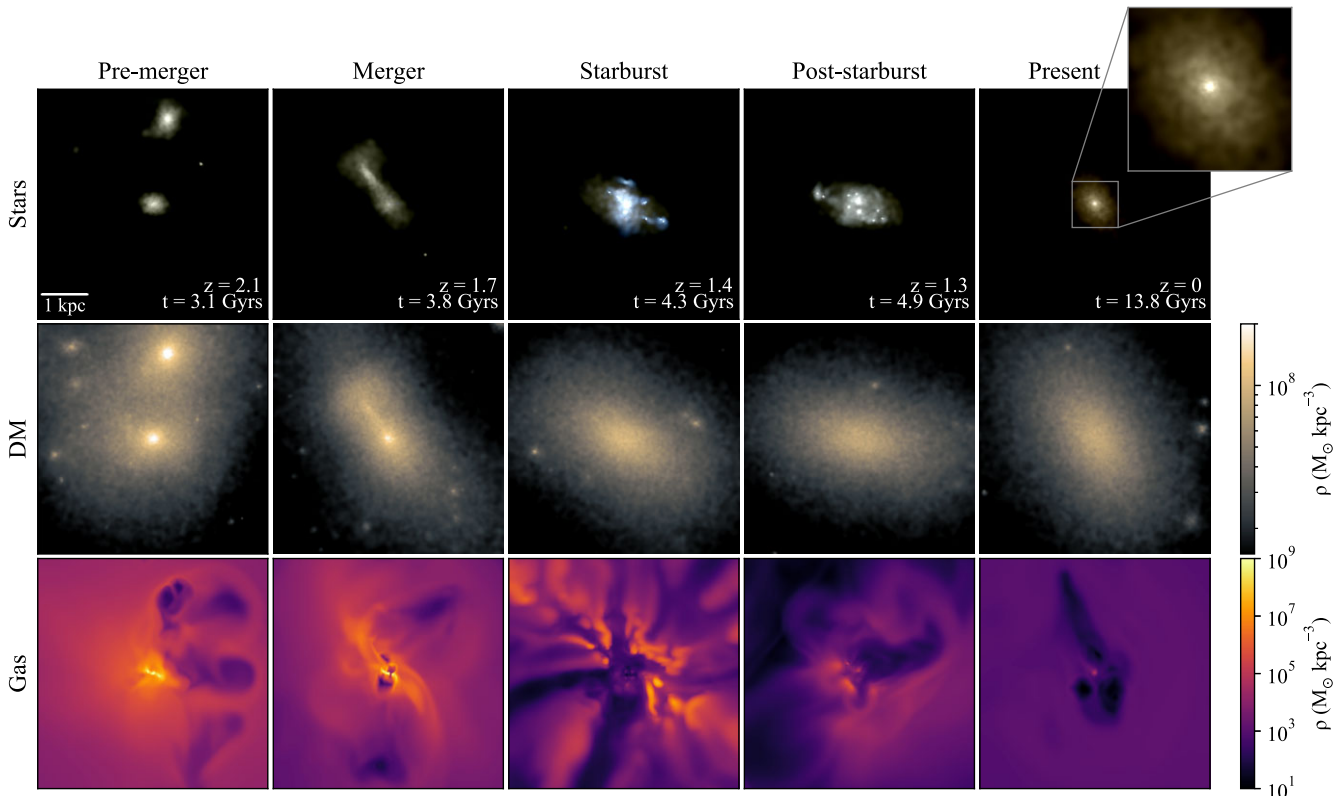


Figure 2. A new mechanism for forming NSCs in low-mass DGs. The panels show the stars (top row), dark matter mass density (middle row), and gas mass density in a 0.1 kpc slice along the z -direction (bottom row) of the Reference simulation for multiple snapshots centred on the main halo. The stars are shown using RGB images in the range 23–28 mag arcsec $^{-2}$ in which the red, blue, and green channels are weighted by the I, V, and U bands, respectively. The panels show the major merger event, which is representative of all the simulations that form an NSC. As the $\sim 1:1$ merger merges with the main halo, the gas builds up and is pushed above the star formation threshold, triggering a giant starburst – visible as bright blue stars. At the same time, this drives a significant gas blowout (see the middle column). This starburst forms small clusters that fall to the galaxy’s centre, forming the NSC.

of the gas density in a 20 kpc box, and gas phase diagrams, for the Reference (top two rows) and Earlier former (bottom two rows).

In both cases, as the merger begins, it compresses the halo gas and allows it to begin cooling. In Reference, this begins to fill a central gas reservoir, which lies above the density threshold but is not yet cool enough to trigger star formation (first panel). This is due to a combination of reionization shutting off the supply of cold star-forming gas and feedback from old stars (AGB winds and Type Ia supernova; Rey et al. 2020), keeping the existing gas too hot for it to cool and form stars. It is only after the major merger has fully completed that this central density can increase even further, exciting a cooling instability (second panel). All the gas in the reservoir is then able to suddenly form stars, resulting in a significant starburst in which the NSC forms (third panel). The resulting large blowout of hot gas from the starburst can be seen in the final panel.

By contrast, the Earlier former, being modified to be more massive at these early times, can induce cooling and continuously form stars throughout its merger (Rey et al. 2020). As a result, it does not form a reservoir of gas. The lack of a dense gas reservoir makes its merger-induced starburst much less dramatic than in the other simulations (with a peak SFR \sim an order of magnitude less, see Fig. 4 top panel). As a result, it does not form an NSC. Of all the simulations, only the Earlier former is able to reignite star formation after its major merger. This is due to the fact that it has a weaker starburst.

Our formation mechanism relies on the formation of a central dense gas reservoir. To build this reservoir, the supply of cold gas before the merger must be halted (through reionization quenching), while feedback from old stars keeps the existing gas hot. Thus,

whether or not a galaxy is able to form an NSC this way is ultimately dictated by the halo’s mass at reionization.

3.3 Observational properties

In this section, we characterize our NSCs in more detail, presenting mock colour–magnitude diagrams (CMDs; Section 3.3.1), metallicities and abundances (Section 3.3.2), and stellar kinematics (Section 3.3.3). We define the NSCs spatially as containing all stars within 4 NSC half-light radii, similarly to observed NSCs. This means that the NSCs will contain both ‘pre-reionization’ and ‘starburst’ stars. However, for some plots we choose to select stars out to an extended radius of 400 pc. This is due to the finite mass resolution of our simulations that leads to undersampling of the pre-reionization stars at small radii.

3.3.1 Colour–magnitude diagrams

In Fig. 6, we show mock CMDs for the Reference dwarf, coloured by both density (left), star age, and [Fe/H] (right). To generate these, we used the `PY-ANANKE` (Thob et al. 2023) code, which utilizes star particle data from cosmological simulations to generate synthetic photometric data. We select data (including positions, velocities, ages, masses, and [Fe/H]) for stars within radii < 400 pc of the galactic centre. We use the *Gaia* photometric system and do not include any photometric uncertainties within our CMD plots.

The Reference NSC has two main sequence turn-offs that owe, primarily, to a distinct separation in age for the pre-reionization

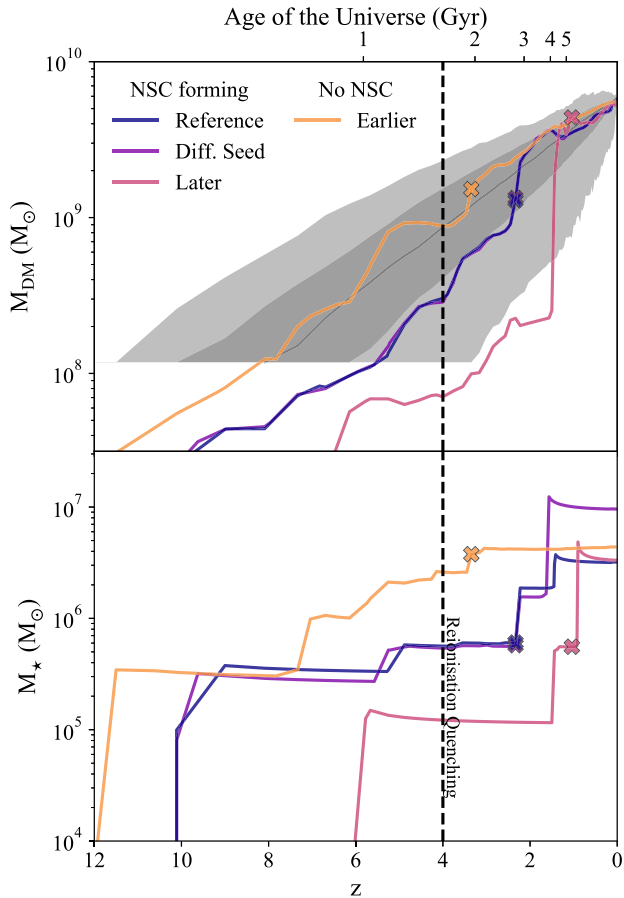


Figure 3. Top panel: the evolution of the total DM mass within the virial radius for all of the simulations (see the legend and Table 1 for a description of each simulation). The grey bands in the top panel show the 68 per cent and 95 per cent confidence intervals of the mass assembly trajectories of all subhaloes in the full EDGE volume. The Earlier simulation reaches a mass threshold at which it can continue to form stars through reionization by $z = 4$. Bottom panel: the evolution of the total stellar mass within the virial radius for all the simulations. The crosses indicate the time the virial radius of the major merger crossed that of the host galaxy and begins the merger event. The vertical dashed line marks the epoch of reionization quenching.

(~ 13 Gyr) and starburst (~ 9.5 Gyr) stellar populations (bottom panel). While the pre-reionization stars are more metal-poor and the starburst population is more metal-rich, this has a more minor impact on the CMD. The other NSCs behave similarly and so we omit these for brevity. A key result of our model is that all NSCs formed in this way should contain at least two stellar populations in their CMDs separated by age and therefore at least two distinct main sequence turn-offs.

As we move outwards from the dwarf’s centre, the younger starburst population becomes less prominent and the main sequence associated with the, more spatially extended, older pre-reionization stellar population increasingly dominates the CMD. We discuss this further, and how some nearby GCs exhibit similar behaviour, in Section 4.

3.3.2 Chemical composition

EDGE also allows us to characterize the oxygen and iron abundances of our simulated dwarfs and NSCs. In Fig. 7, we show the abundance

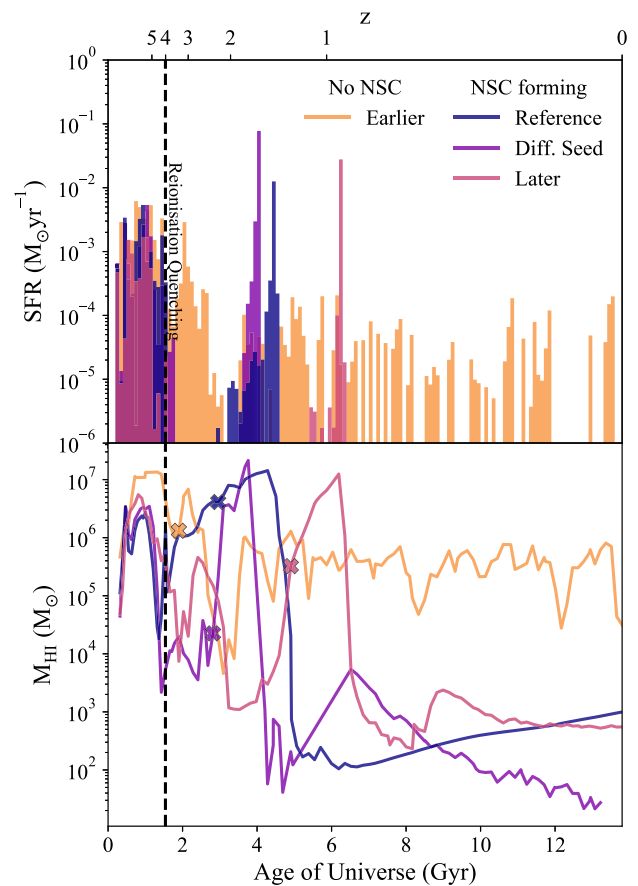


Figure 4. Top panel: star formation history. Bottom panel: H I gas mass evolution. The crosses indicate the beginning of the major merger event in each case. The Reference, Different Seed, and Later simulations all have early star formation, which then quenches due to reionization. A significant merger event causes a build-up of gas, which then excites a NSC-forming starburst, subsequently self-quenching the galaxy. By contrast, the Early simulation does not form an NSC and has continuous star formation.

ratios of oxygen relative to iron as a function of $[\text{Fe}/\text{H}]$, as well as the distributions of both $[\text{Fe}/\text{H}]$ and $[\text{O}/\text{Fe}]$, for each of our simulated nucleated dwarfs. The pre-reionization and starburst stellar populations are shown in blue and red, respectively. Overall, there is an anticorrelation between $[\text{O}/\text{Fe}]$ and $[\text{Fe}/\text{H}]$ due to Type Ia supernovae, during and after the pre-reionization star formation, enriching the to-be-star-forming gas with iron and lowering the $[\text{O}/\text{Fe}]$. This is consistent with metal-complex clusters where iron-rich stars tend to be depleted in oxygen. However, our EDGE dwarfs display a positive correlation for the post-reionization population at more metal-rich $[\text{Fe}/\text{H}]$ values. This is due to the starburst occurring too quickly for Type Ia supernova to significantly contribute, thus causing the gas to rapidly reach high $[\text{O}/\text{Fe}]$ found in typical core-collapse supernova ejecta.

All $[\text{Fe}/\text{H}]$ distributions contain a significant peak, with a tail towards higher values that enhances the average iron abundance values. Such $[\text{Fe}/\text{H}]$ distributions are similar to those observed in massive nearby GCs like Omega Centauri (OC; e.g. Johnson & Pilachowski 2010). While the peaks of the Reference and Different Seed are at similar metallicities, around -2.0 dex, the Later simulation peaks at an $[\text{Fe}/\text{H}]$ value closer to -2.5 dex. This is expected because the Later simulation forms fewer pre-reionization

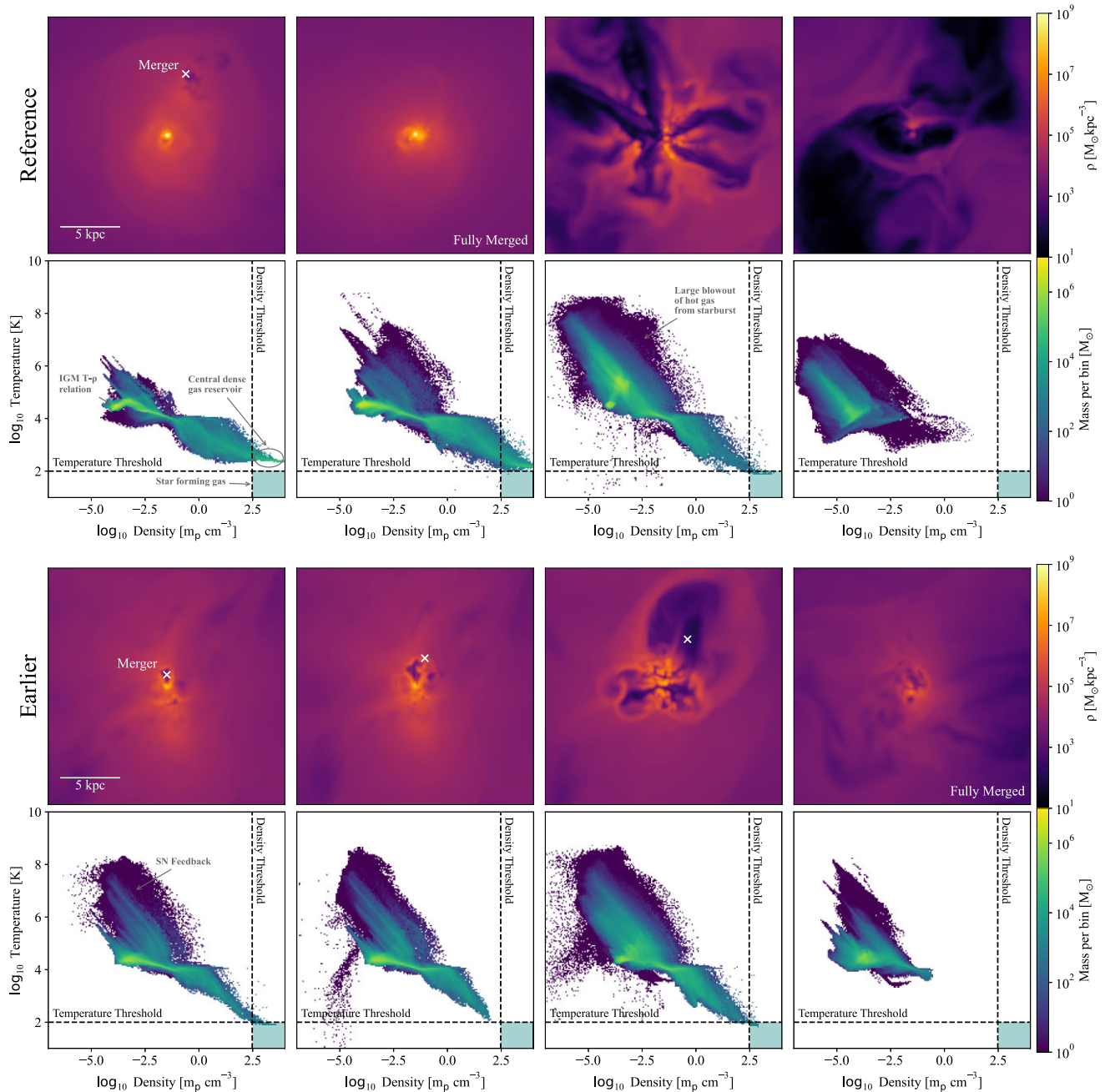


Figure 5. Gas distributions at key output times in the Reference and Earlier simulations: prior to the major merger (left), before (middle left), during (middle right), and after (right) the starburst. The top panels for each simulation show the gas density in a 20 kpc^2 box centred on the main halo. If the major merger has not fully merged, its position is shown by a white cross. The bottom panels show phase diagrams of all gas within the virial radius of the main halo, weighted by gas mass. We mark the temperature and density thresholds required for star formation by black dashed lines. The shaded teal rectangles indicate the star-forming regions – gas here can form stars (where $T_{\text{gas}} < 100 \text{ K}$ and $\rho_{\text{gas}} > 300 \text{ m}_p \text{ cm}^{-3}$). Key features are annotated. Before the starburst, the Reference simulation builds up a dense central gas reservoir that, despite being above the density threshold, is only able to cool and form stars after the merger. The following snapshot shows a significant blowout of hot gas from the resulting starburst (in which an NSC forms). By comparison, dense gas in the Earlier simulation continually cools to form stars, preventing gas build-up. This leads to a much more mild merger-induced starburst. As a result, no NSC forms, while star formation is able to continue through to the present day.

stars (see Fig. 4 bottom panel) and therefore has a lower $[\text{Fe}/\text{H}]$ before its starburst. The $[\text{Fe}/\text{H}]$ values are systematically lower than expected from literature trends for local volume dwarfs of similar magnitudes (Simon 2019). This is most likely due to a combination of lower supernova yields (Woosley & Weaver 1995) and the lack of an explicit model for radiative transfer, which produces

less violent outflows, increasing metal retention (e.g. Agertz et al. 2020). The Different Seed simulation has the highest iron peak value and the smallest spread. This owes to its extremely short, violent, starburst as compared to the other simulations – see Fig. 4. As all of our simulated nucleated dwarfs have only one $[\text{Fe}/\text{H}]$ peak, the split populations that naturally arise in our new NSC

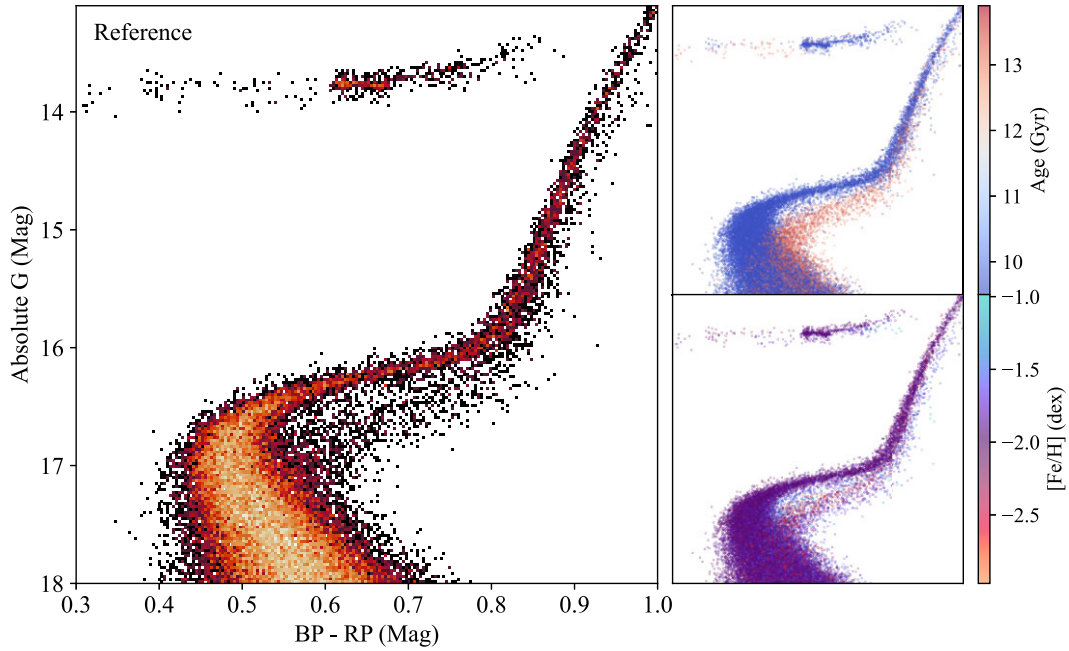


Figure 6. Mock CMDs of the Reference simulation coloured by density (left), stellar age, and [Fe/H] (right). The synthetic photometric data were generated using the `PY-ANANKE` (Thob et al. 2023) code using star particle data within 400 pc of the galaxy’s centre. The *Gaia* photometric system is used with no added photometric errors. The two stellar populations within the EDGE dwarf result in two clear main-sequence turn-offs, primarily due to a distinct separation in age.

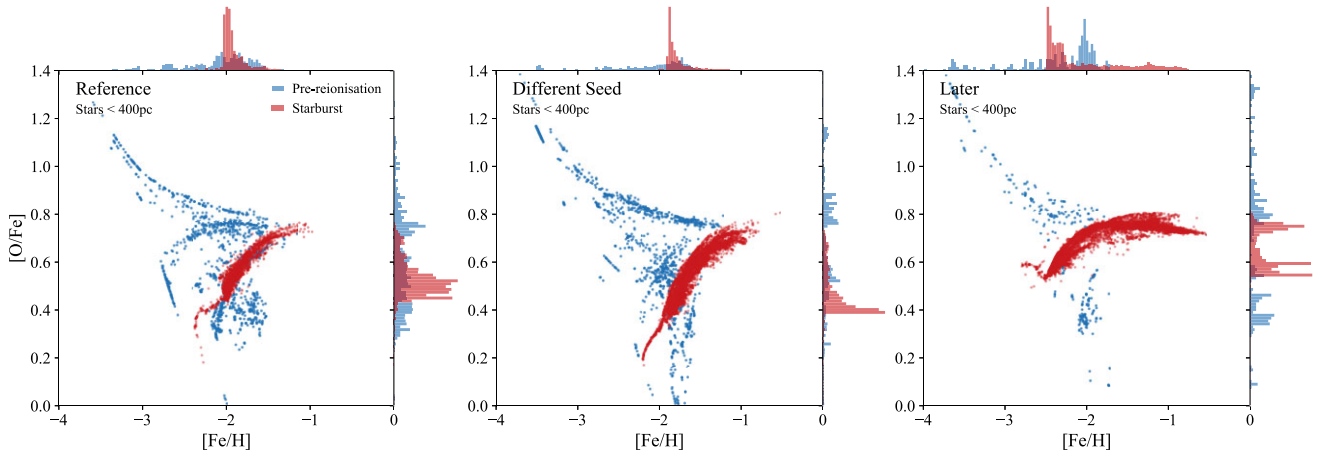


Figure 7. Abundance ratios of oxygen relative to iron as a function of [Fe/H] for stars within 400 pc of all NSC-forming dwarfs. The pre-reionization and starburst populations are coloured by blue and red, respectively. [Fe/H] and [O/Fe] distributions for both populations are displayed above and to the right of the centre plot, respectively. The pre-reionization population displays an anticorrelation in contrast to the younger starburst population.

formation mechanism are not discernible from [Fe/H] measurements alone.

Our dwarfs display complex [O/Fe] distributions, with some containing multiple peaks – even within just the starburst population. This is due to the sensitivity of oxygen abundances to the local star formation conditions. All simulations display at least one epoch of rapid enrichment during the starburst event, causing a sudden increase of ~ 0.2 dex in [O/Fe]. The Reference and Different Seed simulations contain multiple such epochs of rapid enrichment, each distinct in time and space. This leads to a broader [O/Fe] spread. The starburst population for the Later simulation displays three clear peaks. The two peaks at < 0.6 dex correspond to spatially distinct star-forming regions that have distinct [O/Fe]. Stars forming from

the gas enriched by these two star-forming regions then produces the third, broader, [O/Fe] peak at ~ 0.7 dex.

3.3.3 Stellar kinematics

In this section, we separate the two stellar populations in our simulated NSCs based on their formation epochs: pre-reionization and starburst. This allows us to investigate differences in their kinematic properties that could be tested observationally. Fig. 8 (left and middle panels) shows the radial and tangential velocity dispersions as a function of radius for the stars created before reionization quenching and the stars created within the NSC-forming starburst. Notice that the older stellar population is kinematically hotter than the starburst

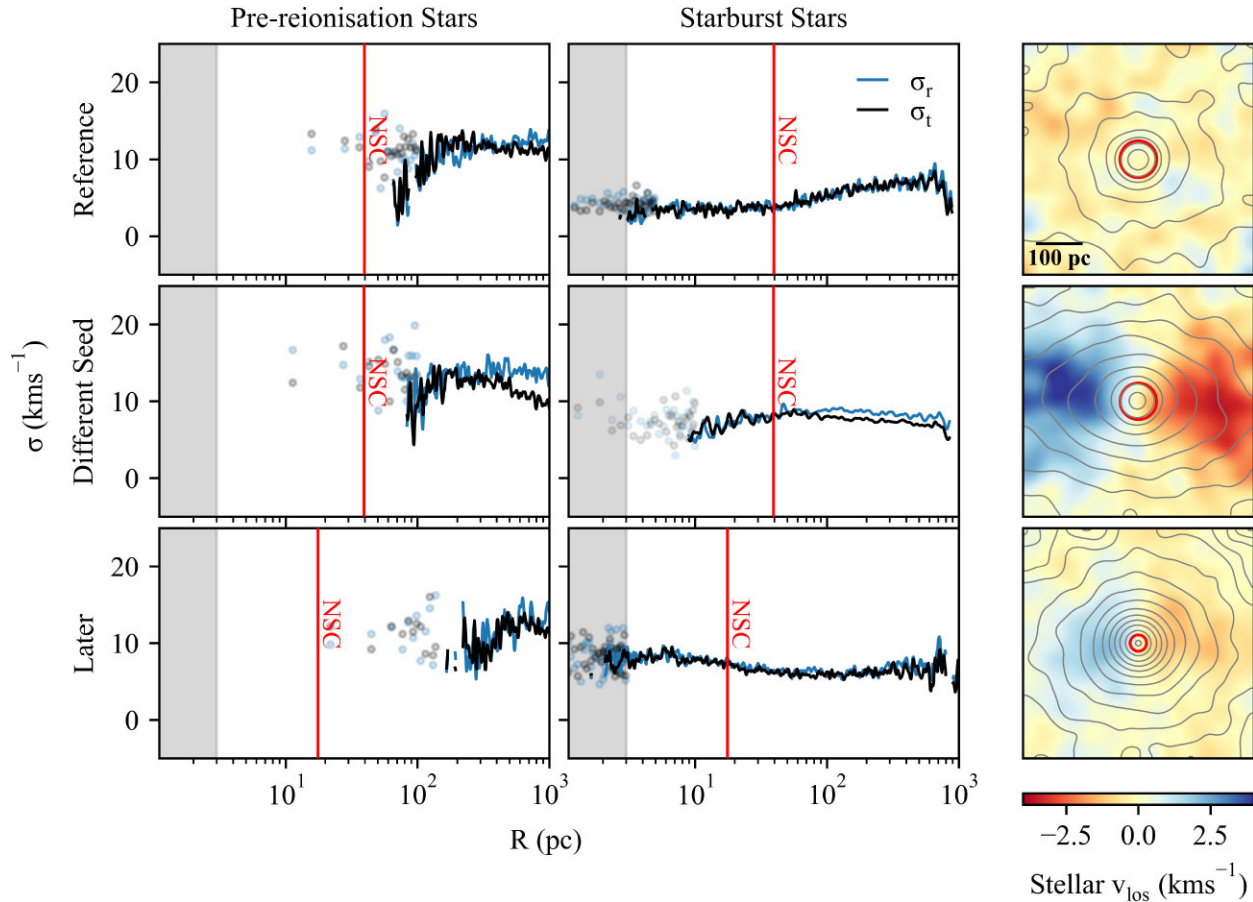


Figure 8. The radial (blue) and tangential (black) stellar velocity dispersions for the Reference, Different Seed, and Later simulations (at $z = 0$) for the stars formed before reionization quenching (left; < 2.5 Gyr from the start of the simulation), and stars formed during the starburst (right; > 2.5 Gyr from the start of the simulation). In both cases, we align the dwarf ‘face on’ such that the direction of the angular momentum vector of stars $< \text{NSC}$ radii from the dwarf’s centre is along the z -axis. Radial bins are equal in the log scale. At smaller radii, we add data points with an equal number of stars in each bin (~ 10 star particles). The grey band to the left of the plot marks the simulation spatial resolution of 3 pc. The third column shows projected velocity maps of the Reference, Different Seed, and Later nucleated dwarfs at $z = 0$ covering an area of 1 kpc. For each radial bin the average stellar velocity in the z -direction was found for all stars within the virial radius of the simulated dwarfs. Each dwarf was aligned ‘side on’. The contours represent stellar densities. The Different Seed simulation displays the strongest rotation, with a rotational velocity that reaches 4 km s^{-1} at 100–200 pc from the dwarf’s centre. The Later simulation shows a much weaker rotation, while the Reference simulation has no detectable rotation signal. The red vertical line denotes the NSC radii in each case. This plot makes a clear prediction that, if an object is formed in this way, when sliced on the two populations, one is kinematically hotter than the other.

population. This difference in velocity dispersions could serve as an observational test as to whether a galaxy has an NSC formed in a way similar to our model.

Fig. 8 also shows that two out of three of our simulated NSCs are rotating. The right panels show 2D line-of-light velocity maps of all stars, oriented ‘side-on’. The Different Seed simulation is rotating, rising above an amplitude of $\sim 2.5 \text{ km s}^{-1}$, while the Later simulation also shows some weak evidence of rotation. In both cases, the rotation signal becomes most prominent at distances of ~ 100 – 200 pc from the dwarf’s centre, far beyond the NSC’s half light radius. However, it can still, at least in principle, provide another observational test of our NSC formation scenario.

4 DISCUSSION

4.1 Model limitations

In this section, we discuss the dependency of our results on the sub-grid physics choices in the EDGE simulations. Our NSC formation

mechanism relies on the sufficient suppression of star formation from cosmic reionization. The mass-scale at which this occurs is sensitive to the detailed balance between heating and cooling after reionization (e.g. Benitez-Llambay & Frenk 2020; Rey et al. 2020 and references therein). Cooling will be enhanced in DGs with higher metal retention, for example. This can occur due to the inclusion of explicit photoionization feedback that enhances metal retention (Agertz et al. 2020), or due to reasonable changes in the stellar yield model (e.g. Pillepich et al. 2018). Furthermore, key heating terms are uncertain, including the strength of the UV background after reionization (UVB; e.g. Khaire & Srianand 2019; Puchwein et al. 2019; Faucher-Giguère 2020) or the importance of stellar feedback from evolved binary stars (Rey et al. 2020). None the less, we argue that all these uncertainties only act to shift the absolute mass-scale at which our NSC formation mechanism occurs. For example, a stronger UVB than is assumed here would push reionization-driven quenching, and therefore the mass scale at which dwarfs can form NSCs via this mechanism, to higher mass. [Indeed, merger-driven nuclear starbursts are well established in galaxy formation theory

(Springel, di Matteo & Hernquist 2005; Renaud, Segovia Otero & Agertz 2022), highlighting their robustness to sub-grid physics choices.]

Despite our EDGE simulations being able to resolve individual supernovae explosions, the simulations presented in this work do not account for radiative feedback from young stars. Since photoionization and photoheating from stars are active as soon as they are born, this feedback channel helps regulate starbursts and makes feedback less bursty and explosive in dwarfs (Ageretz et al. 2020; Smith et al. 2021). It remains to be seen how the nuclear starburst forming the NSC would proceed when including these additional physical effects. We will quantify this in future work.

Finally, it is also crucial to consider the impact of different random number seeds on our results. We tested this with the ‘Reference’ and ‘Different Seed’ simulations. These have nearly identical initial conditions that lead to nearly identical dark matter halo density profiles throughout the simulations. There is good qualitative agreement between the two simulations in their star formation histories (see Fig. 4), particularly before reionization. However, the post-reionization starburst is particularly sensitive to stochastic processes in our sub-grid star formation and stellar feedback models (see Section 2). This leads to Different Seed having a higher and narrower starburst that leads to an NSC that has a similar size to Reference, but is approximately five times more massive (see Table 1). Such stochasticity may be unavoidable, at least at the numerical resolution of our EDGE simulations. It means that it is challenging for us to accurately predict NSC properties, at least on a galaxy-by-galaxy basis. We will explore this further in future work.

4.2 NSC formation across simulation studies

In our simulations, NSCs form within DGs with host stellar masses $\sim 10^6 M_\odot$ where the most dominant formation scenario is often thought to be GC infall (e.g. Fahrion et al. 2022b). Previous observations of dwarf NSCs, which tend to be more metal-poor than their surrounding galaxies, support this scenario as the properties of these NSCs align with those expected from accreted GCs. A detailed comparison of the observational properties of our simulated NSCs with real observations is provided in Section 4.3.

However, our NSC formation scenario aligns more closely with the alternative *in situ* star formation mechanism. *In situ* formation triggered by a major merger is not a new concept and has been previously proposed in the context of larger galaxies. Early numerical models, such as those by Mihos & Hernquist (1994), demonstrated NSC formation following the merger of gas-rich disc galaxies. More recent studies, such as the high-resolution GigaEris simulation of an MW-sized galaxy (Donkelaar et al. 2024), suggest a hybrid formation scenario involving both *in situ* star formation and the accretion of gas-rich stellar clusters. The primary distinction between these MW-sized simulations and our DG model is that while Donkelaar et al.’s (2024) NSC formation relies on periodic *in situ* star formation driven by bar-driven gas inflows, our dwarf NSCs form through a single, intense starburst triggered by a major merger. This starburst then quenches further star formation.

Other studies also propose wet merger scenarios for NSC formation in dwarfs. For example, Guillard et al. (2016) use hydrodynamical simulations of isolated gas-rich dwarfs (with stellar masses $\sim 10^9 M_\odot$ and total masses of $\sim 10^{11} M_\odot$) to show that star clusters with gas reservoirs can form in the disc and migrate to the galactic centre via dynamical friction, forming NSCs. As with the other studies above, the host dwarfs in Guillard et al. (2016) are more massive than those in our EDGE simulations, which focus on

lower mass dwarfs (with stellar mass, $\sim 10^6 M_\odot$ and total mass, $\sim 10^9 M_\odot$).

A key distinction of our new NSC formation mechanism, as compared to these earlier works, is that an additional condition is required for NSC formation, extra to a major merger. Sufficient quenching of star formation due to reionization is necessary prior to the merger, so that it is able to build up central gas mass. This is only possible for DGs that are quenched by reionization, making our mechanism unique to low-mass dwarfs.

There is a notable lack of high-resolution simulations of DGs similar in mass to those in our study that include the formation of clusters in a fully cosmological environment. The LYRA simulations (Gutcke et al. 2022b), which are the most comparable, achieve even higher resolution than EDGE for a smaller number of simulated dwarfs. There are key differences in our sub-grid models that likely drive differences between our studies (LYRA does not include, for example, stellar winds). Almost all LYRA dwarfs are nucleated, which is in tension with observational data (e.g. Poulain et al. 2021). The mechanism(s) for forming nuclei in LYRA have not yet been explicitly discussed.

4.3 A new mechanism for forming NSCs

We have presented a new mechanism for forming NSCs (with stellar mass $M_* \sim 0.3 - 1.3 \times 10^6 M_\odot$) in low-mass DGs ($M_{200c} \sim 5 \times 10^9 M_\odot$). Our model makes a number of key observational predictions:

- (i) The NSCs should have (at least) two distinct stellar populations with a large separation (~ 1 Gyr) in age. This yields a CMD with two (or more) distinct main sequence turn-offs.
- (ii) The younger NSC population should be more metal-rich than the older population.
- (iii) The younger NSC population should be kinematically colder than the older population.
- (iv) The younger NSC population should be more spatially compact than the older population.

Ideally, we should compare our EDGE model predictions to isolated nucleated dwarfs in low-density environments. Our model predicts that massive NSCs can form in dwarfs with stellar masses in the range $\sim 3-10 \times 10^6 M_\odot$. We are beginning to explore such nucleated dwarfs in low-density environments through new surveys like MATLAS (Poulain et al. 2021). However, the best-studied nucleated dwarfs to date are in cluster environments, for example, the Virgo cluster (e.g. Sánchez-Janssen et al. 2019) and the Fornax cluster (e.g. Turner et al. 2012). This creates additional complexity when making model comparisons because of the impact of tides, environment quenching, and environmentally driven morphological transformations.

Several dwarfs in the Virgo cluster have a similar stellar mass to our dwarfs while also containing an NSC, with the smallest of these having a total stellar mass of $M_* = 10^{5.2} M_\odot$ containing an $M_* = 10^{4.8} M_\odot$ NSC (Sánchez-Janssen et al. 2019). The ratio of total galaxy stellar mass to NSC stellar mass on average for these is higher than our dwarfs, indicating some tidal stripping of the host galaxy has likely decreased its total stellar mass. There are a couple that are more similar to our simulated dwarfs (e.g. NGVS J12:26:51.99+12:39:08.2 and NGVS J12:28:59.15+12:02:30.4); however, it is difficult to know for certain if these could be formed in a similar way to our dwarfs due to the denser environment. Similarly, both KK58 ($M_* = 7.8 \times 10^6 M_\odot$) and KK197 ($M_* = 4 \times 10^7 M_\odot$) within the Centaurus group have NSCs of stellar mass of $M_* =$

$7.3 \times 10^5 M_{\odot}$ and $1.0 \times 10^6 M_{\odot}$, respectively (Fahrion et al. 2020). However, in both cases the NSCs are more metal-poor ($[Fe/H] = -1.75 \pm 0.06$ dex and -1.84 ± 0.05 dex for KKs58 and KK197, respectively) than the host galaxy ($[Fe/H] = -1.35 \pm 0.23$ dex and -0.84 ± 0.12 dex for KKs58 and KK197, respectively). This could favour a GC inspiral scenario acting instead of, or in tandem, with the mechanism we present here, or point to continued star formation after the NSC forms that raises the metallicity of the host dwarf.

4.4 Could some nearby GCs actually be accreted NSCs?

Several studies in the literature have proposed that at least some GCs in the Milky Way might actually be NSCs accreted from now-dissolved nucleated dwarfs (e.g. Freeman 1993; Böker 2007). These arguments include evidence of significant iron spreads in some GC-NSC candidates (Da Costa 2016; Pfeffer et al. 2021), and the presence of distinct populations in the CMDs (e.g. Carretta et al. 2010). For instance, Pfeffer et al. (2021) identify NGC 6723 as a candidate NSC for Kraken based on its complex chemical and kinematic properties, including multiple stellar populations with varied metallicity.

Here, we focus on a subset of GCs that show photometrically distinct main-sequence turn-offs, specifically the Type II GCs from Milone et al. (2017). Our model suggests that these GCs could be accreted NSCs. (To avoid confusion, the term ‘multiple main-sequence turn-offs’ is used in this paper, which refers specifically to the distinct main-sequence turn-offs observed in the CMD). This is distinct from the broader term ‘multiple stellar populations’, which, in the context of GCs, often includes chemical abundance anomalies (e.g. Bastian & Lardo 2018.) One of the Type II GCs, and also the most likely NSC candidate, is M54, which has long been thought to be the nucleus of the Sagittarius DG (e.g. Siegel et al. 2007; Carretta et al. 2010; Carlberg & Grillmair 2022). M54 shows evidence for multiple split main-sequence turn-offs exactly as predicted by our model (e.g. Alfaro-Cuello et al. 2019). Similarly, OC has long been speculated to be a DG core disrupted from its host galaxy (Hilker & Richtler 2000; Bekki & Freeman 2003; Kuzma, Ferguson & Peñarrubia 2021). It too shows at least three distinct main sequence turn-offs in its CMD (e.g. Bellini et al. 2010).

Alongside these, there are many other ‘split main-sequence turn-off’ GCs that also show a significant iron spread. We have undertaken a census and highlighted these in Fig. 9, which shows the V -band magnitude as a function of half-light radius for observed GCs (grey diamonds) and DGs (green diamonds) as compared to our EDGE NSCs. Notice that our EDGE NSCs lie within the region occupied by bright GCs, particularly those identified as having clear split main-sequence turn-offs. We speculate that many of these GCs could be accreted NSCs that formed through the new mechanism presented here.

We can further test our NSC accretion hypothesis by comparing the spatial distributions, kinematics, and chemical compositions of the split populations in our model. Our model predicts that the pre-ionization and starburst populations should be distinct, with the older stars occupying a separate, redder, main sequence (Fig. 6). The older stars are also kinematically hotter (Fig. 8), more metal-poor (Fig. 7), and more extended than the younger NSC stars. It is challenging to compare these predictions in detail with nearby GCs like M54 and OC because nearby GCs: (i) have experienced significant tidal forces that we do not model in our EDGE simulations (e.g. Kuzma et al. 2021); (ii) they undergo important two-body effects like mass segregation and evaporation that are not captured in EDGE (e.g. Dehnen & Read 2011; Zocchi, Gieles & Hénault-Brunet 2019);

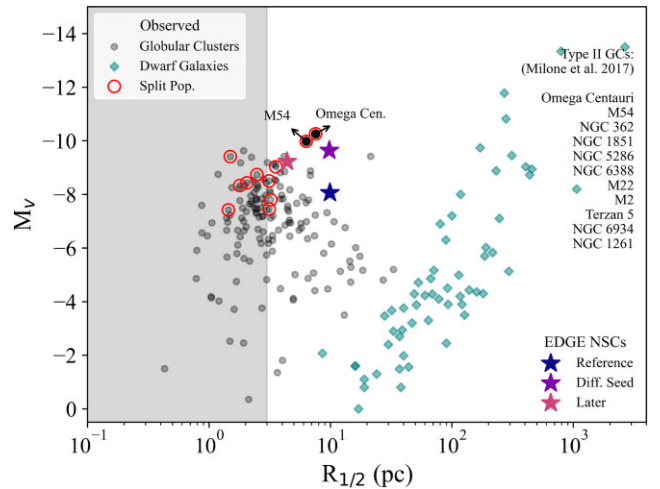


Figure 9. V -band magnitude as a function of the half-light radius. The EDGE NSC data are displayed in large star symbols – the V -band magnitude for these has been calculated from the stars within 4 NSC half-light radii. Observational data for both GCs (Harris 2010; Laevens et al. 2015; Crnojević et al. 2016; Cerny et al. 2023) and DGs (Conn et al. 2018; Simon 2019; Collins et al. 2022, 2024; Sand et al. 2022; McQuinn et al. 2023) are shown in grey circles and teal diamonds, respectively. GCs identified as Type II from Milone et al. 2017 are circled in red and listed on the right of the plot. These include the clusters OC and M54 (Siegel et al. 2007), which are directly labelled, in addition to Terzan 5 (Ferraro et al. 2009), NGC 1851, M22, NGC 5286, M2, NGC 362, NGC 1261, NGC 6388, and NGC 6934 (Piotto et al. 2012; Milone et al. 2017). The grey band to the left of the plot marks the simulation spatial resolution of 3 pc.

and (iii) both M54 and OC have more than two main sequences and so have lived more complex lives than our simulated NSCs. Note that this latter point is not a problem for our model. Given the low halo mass in which our NSCs form, we can expect that they will accrete on to larger galaxies where they will sink to the centre, merging with other GCs and NSCs and possibly undergoing additional star formation through further gas cooling. Such processes will add further complexity to their observed properties today.

With the above caveats in mind, we now compare our NSC model to two well-studied GCs that are among the most likely to be NSCs: M54 and OC. M54 displays very similar qualitative behaviour to our model predictions. Alfaro-Cuello et al. (2020) report that the younger stars are kinematically colder and more metal-rich than the older population, exactly as our model predicts, while Alfaro-Cuello et al. (2019) show that the younger stars are more centrally concentrated than the intermediate-age stars (that they attribute to the host galaxy–Sagittarius). The discussion surrounding OC is more complicated, with some studies agreeing that the apparently ‘older’, redder, main sequence is more metal-poor than the ‘younger’, bluer, one (Piotto et al. 2005; Latour et al. 2021), while others appearing to show the opposite (Calamida et al. 2017; Nitschai et al. 2023). Some studies report more centrally concentrated metal-poor stars (Calamida et al. 2020), which contrast with others who claim a central metal-rich component (van de Ven et al. 2006). Many studies find that the multiple populations can be reasonably explained by a large spread in metallicity rather than age (e.g. Tailo et al. 2016).

Finally, we can look at rotation. Both OC and M54 show clear signs of rotation of magnitude $5\text{--}10 \text{ km s}^{-1}$, particularly in the younger stellar populations (Merritt, Meylan & Mayor 1996; Alfaro-Cuello et al. 2020). Some of our NSCs show a similar rotation amplitude (e.g. reaching $\sim 4 \text{ km s}^{-1}$ for the Different Seed simulation), but on

larger radial scales [100–200 pc as compared to ~ 10 pc for OC and M54 (Merritt et al. 1996; Alfaro-Cuello et al. 2020)]. This difference may owe to the additional complexity seen in both M54 and OC as compared to our model. For M54 at least, there is a younger population that could have formed from further gas dissipation and collapse that could then be more highly rotating (e.g. Alfaro-Cuello et al. 2020). However, it is important to note that we struggle to resolve rotation on sub-10 pc scales given that our finest resolution cells are of size 3 pc. As such, we will return to this point with higher resolution simulations in future work.

5 CONCLUSIONS

Using a suite of high-resolution simulations of DGs drawn from the EDGE project (~ 3 pc spatial resolution), we have uncovered a new formation mechanism for NSCs. We find that massive NSCs ($M_* (< 4r_{1/2}) \sim 8 \pm 4 \times 10^5 M_\odot$) can form in surprisingly low halo mass DGs ($M_{200c} \sim 5 \times 10^9 M_\odot$ at $z = 0$) at high redshift ($z \sim 2$). Our formation mechanism proceeds, as follows. First, the EDGE dwarf is sufficiently low mass that it is quenched by reionization. Next, at some point after reionization, the dwarf undergoes a major $\sim 1:1$ merger, causing the formation of a dense central gas reservoir. Once the merger has fully completed, rapid cooling of this reservoir leads to a major starburst. The NSC forms in the starburst that quenches star formation thereafter. This process naturally results in two stellar populations that have a \sim billion year age-gap and mock CMD that resembles some nearby GCs like OC and M54 that have multiple, distinct, main-sequence turn-offs. Further work will be required to quantify what fraction of NSCs form through this mechanism. Note in particular that other mechanisms may dominate at higher masses, far from the reionization scale.

We went on to study the detailed observational properties of our simulated NSCs, including their surface brightness, chemical composition, mock CMDs, and stellar kinematics. Our key results are as follows:

(i) All of the surface brightness profiles for our nucleated EDGE dwarfs can be fit using two Sérsic profiles, one which corresponds to the NSC and the other to the host galaxy.

(ii) Mock CMDs of the inner stellar populations display clear split main-sequence turn-offs due to the large ($\gtrsim 1$ billion year) age separation in the pre-reionization and starburst stellar populations. Such split populations have already been observed in many bright GCs in the Milky Way. Our model suggests that these clusters, especially those that also have a significant [Fe/H] spread, could be accreted NSCs.

(iii) The average [Fe/H] and [O/Fe] of our simulated NSCs are $\sim -2 \pm 0.1$ dex and 0.5 ± 0.1 dex, respectively. We qualitatively reproduce both the anticorrelation between iron and oxygen found in GCs that show significant [Fe/H] spread, and the overall shape of the [Fe/H] distribution.

(iv) Our pre-reionization and starburst stellar populations are distinct, with the older pre-reionization population being kinematically hotter. This could serve as an observational indicator as to whether a galaxy has an NSC formed in a similar way to our model.

ACKNOWLEDGEMENTS

We would like to thank the anonymous referee for a constructive review that improved the quality of the manuscript. The authors would like to thank Dr Santi Cassisi and Dr Alex Riley for their sup-

port with synthetic CMD tools, as well as Madeleine McKenzie and Oliver Camilleri for the useful feedback and interesting discussions.

This project has received funding from the European Union's Horizon 2020 research and innovation programme under grant agreement No. 818085 GMGalaxies. JIR would like to thank the STFC for support from grants ST/Y002865/1 and ST/Y002857/1. ET acknowledges the UKRI Science and Technology Facilities Council (STFC) for support (grant ST/V50712X/1). MO acknowledges funding from the European Research Council (ERC) under the European Union's Horizon 2020 research and innovation programme (grant agreement No. 852839). MR is supported by the Beecroft Fellowship funded by Adrian Beecroft. OA acknowledges support from the Knut and Alice Wallenberg Foundation, the Swedish Research Council (grant 2019-04659), and the Swedish National Space Agency (SNSA Dnr 2023-00164).

This work also used the DiRAC@Durham (cosma6) facility managed by the Institute for Computational Cosmology on behalf of the STFC DiRAC HPC Facility (www.dirac.ac.uk). The equipment was funded by BEIS capital funding via STFC capital grants ST/P002293/1, ST/R002371/1, and ST/S002502/1, Durham University, and STFC operations grant ST/R000832/1. DiRAC is part of the National e-Infrastructure.

DATA AVAILABILITY

Data available upon reasonable request.

REFERENCES

- Agertz O., Kravtsov A. V., Leitner S. N., Gnedin N. Y., 2013, *ApJ*, 770, 25
 Agertz O. et al., 2020, *MNRAS*, 491, 1656
 Alfaro-Cuello M. et al., 2019, *ApJ*, 886, 57
 Alfaro-Cuello M. et al., 2020, *ApJ*, 892, 20
 Antonini F., Barausse E., Silk J., 2015, *ApJ*, 812, 72
 Antonini F., Gieles M., Gualandris A., 2019, *MNRAS*, 486, 5008
 Bastian N., Lardo C., 2018, *ARA&A*, 56, 83
 Bekki K., 2007, *Publ. Astron. Soc. Aust.*, 24, 77
 Bekki K., Freeman K., 2003, *MNRAS*, 346, L11
 Bekki K., Couch W. J., Shioya Y., 2006, *ApJ*, 642, L133
 Bellini A., Bedin L. R., Piotto G., Milone A. P., Marino A. F., Villanova S., 2010, *AJ*, 140, 631
 Bender R. et al., 2005, *ApJ*, 631, 280
 Benítez-Llambay A., Frenk C., 2020, *MNRAS*, 498, 4887
 Böker T., 2007, *ApJ*, 672, L111
 Brown G., Gnedin O. Y., Li H., 2018, *ApJ*, 864, 94
 Calamida A. et al., 2017, *AJ*, 153, 175
 Calamida A. et al., 2020, *ApJ*, 891, 167
 Capuzzo-Dolcetta R., Mastrobuono-Battisti A., 2009, *A&A*, 507, 183
 Capuzzo-Dolcetta R., Miocchi P., 2008, *ApJ*, 681, 1136
 Carlberg R. G., Grillmair C. J., 2022, *ApJ*, 935, 14
 Carlsen S. G., Greene J. E., Beaton R. L., Greco J. P., 2022, *ApJ*, 927, 44
 Carretta E. et al., 2010, *ApJ*, 714, L7
 Carson D. J., Barth A. J., Seth A. C., Den Brok M., Cappellari M., Greene J. E., Ho L. C., Neumayer N., 2015, *ApJ*, 149, 170
 Cerny W. et al., 2023, *ApJ*, 953, L21
 Collins M. L., Read J. I., 2022, *Nat. Astron.*, 6, 647
 Collins M. L., Charles E. J., Martínez-Delgado D., Monelli M., Karim N., Donatiello G., Tollerud E. J., Boschin W., 2022, *MNRAS*, 515, L72
 Collins M. L. et al., 2024, *MNRAS*, 528, 2614
 Conn B. C., Jerjen H., Kim D., Schirmer M., 2018, *ApJ*, 852, 68
 Côté P. et al., 2006, *ApJS*, 165, 57
 Côté P. et al., 2007, *ApJ*, 671, 1456
 Crnojević D., Sand D. J., Zaritsky D., Spekkens K., Willman B., Hargis J., 2016, *ApJ*, 824, L14

- Da Costa G. S., 2016, in Bragaglia A., Arnaboldi M., Rejkuba M., Romano D., eds, Proc. IAU Symp. 317, The General Assembly of Galaxy Halos: Structure, Origin and Evolution. Kluwer, Dordrecht, p. 110
- Dehnen W., Read J. I., 2011, *Eur. Phys. J. Plus*, 126, 55
- Den Brok M. et al., 2014, *MNRAS*, 445, 2385
- Dubois Y., Teyssier R., 2008, *A&A*, 477, 79
- Eisenstein D. J., Hut P., 1998, *ApJ*, 498, 137
- Emsellem E., Van De Ven G., 2008, *ApJ*, 674, 653
- Fahrion K. et al., 2020, *A&A*, 634, A53
- Fahrion K. et al., 2021, *A&A*, 650, A137
- Fahrion K., Leaman R., Lyubenova M., van de Ven G., 2022a, *A&A*, 658, A172
- Fahrion K. et al., 2022b, *A&A*, 667, A101
- Faucher-Giguère C.-A., 2020, *MNRAS*, 493, 1614
- Feldmeier-Krause A. et al., 2015, *A&A*, 584, A2
- Ferrarese L. et al., 2006, *ApJ*, 644, L21
- Ferraro F. et al., 2009, *Nature*, 462, 483
- Freeman K. C., 1993, in Smith G. H., Brodie J. P., eds, ASP Conf. Ser. Vol. 48, The Globular Cluster-Galaxy Connection. Astron. Soc. Pac., San Francisco, p. 608
- Georgiev I. Y., Böker T., 2014, *MNRAS*, 441, 3570
- Gnedin O. Y., Ostriker J. P., Tremaine S., 2014, *ApJ*, 785, 71
- Grisdale K., Agertz O., Renaud F., Romeo A. B., Devriendt J., Slyz A., 2019, *MNRAS*, 486, 5482
- Guillard N., Emsellem E., Renaud F., 2016, *MNRAS*, 461, 3620
- Gutcke T. A., Pakmor R., Naab T., Springel V., 2022a, *MNRAS*, 513, 1372
- Gutcke T. A., Pfrommer C., Bryan G. L., Pakmor R., Springel V., Naab T., 2022b, *ApJ*, 941, 120
- Haardt F., Madau P., 1995, *ApJ*, 461, 20
- Harris W. E., 2010, preprint ([arXiv:1012.3224](https://arxiv.org/abs/1012.3224))
- Hartmann M., Debattista V. P., Seth A., Cappellari M., Quinn T. R., 2011, *MNRAS*, 418, 2697
- Hilker M., Richtler T., 2000, *A&A*, 362, 895
- Hopkins P. F., Quataert E., 2010, *MNRAS*, 407, 1529
- Hoyer N., Neumayer N., Georgiev I. Y., Seth A. C., Greene J. E., 2021, *MNRAS*, 507, 3246
- Johnson C. I., Pilachowski C. A., 2010, *ApJ*, 722, 1373
- Kacharov N., Neumayer N., Seth A. C., Cappellari M., McDermid R., Walcher C. J., Böker T., 2018, *MNRAS*, 480, 1973
- Katz N., White S. D., 1993, *ApJ*, 412, 455
- Kennicutt R. C., Jr, 1998, *ApJ*, 498, 541
- Khaire V., Srikanand R., 2019, *MNRAS*, 484, 4174
- Kimm T., Cen R., Devriendt J., Dubois Y., Slyz A., 2015, *MNRAS*, 451, 2900
- Kuzma P. B., Ferguson A. M. N., Peñarrubia J., 2021, *MNRAS*, 507, 1127
- Laevens B. P. et al., 2015, *ApJ*, 813, 44
- Latour M., Calamida A., Husser T. O., Kamann S., Dreizler S., Brinchmann J., 2021, *A&A*, 653, L8
- Lim S., Peng E. W., Côté P., Sales L. V., den Brok M., Blakeslee J. P., Guhathakurta P., 2018, *ApJ*, 862, 82
- Lotz J. M., Telford R., Ferguson H. C., Miller B. W., Stiavelli M., Mack J., 2001, *ApJ*, 552, 572
- Lu J., Ghez A., Hornstein S. D., Morris M., Becklin E., Matthews K., 2008, *ApJ*, 690, 1463
- McLaughlin D. E., 1999, *ApJ*, 117, 2398
- McQuinn K. B., Mao Y.-Y., Buckley M. R., Shih D., Cohen R. E., Dolphin A. E., 2023, *ApJ*, 944, 14
- Merritt D., Meylan G., Mayor M., 1996, *AJ*, 114, 1074
- Mihos C., Hernquist L., 1994, *ApJ*, 431, L9
- Miller B. W., Lotz J. M., 2007, *ApJ*, 670, 1074
- Milone A. et al., 2017, *MNRAS*, 464, 3636
- Milosavljević M., 2004, *ApJ*, 605, L13
- Neumayer N., Seth A., Böker T., 2020, *A&AR*, 28, 1
- Nguyen D. D. et al., 2019, *ApJ*, 872, 104
- Nitschai M. S. et al., 2023, *ApJ*, 958, 8
- Oñorbe J., Garrison-Kimmel S., Maller A. H., Bullock J. S., Rocha M., Hahn O., 2014, *MNRAS*, 437, 1894
- Orkney M. D. et al., 2021, *MNRAS*, 504, 3509
- Paumard T. et al., 2006, *ApJ*, 643, 1011
- Pfeffer J., Lardo C., Bastian N., Saracino S., Kamann S., 2021, *MNRAS*, 500, 2514
- Pillepich A. et al., 2018, *MNRAS*, 473, 4077
- Piotto G. et al., 2005, *ApJ*, 621, 777
- Piotto G. et al., 2012, *ApJ*, 760, 39
- Planck Collaboration XVI, 2014, *A&A*, 571, A16
- Pontzen A., Tremmel M., 2018, *ApJS*, 237, 23
- Pontzen A., Roškar R., Stinson G., Woods R., 2013, Astrophysics Source Code Library, record ascl:1305.002
- Poulain M. et al., 2021, *MNRAS*, 506, 5494
- Puchwein E., Haardt F., Haehnelt M. G., Madau P., 2019, *MNRAS*, 485, 47
- Rasera Y., Teyssier R., 2006, *A&A*, 445, 1
- Read J., Agertz O., Collins M., 2016, *MNRAS*, 459, 2573
- Renaud F., Segovia Otero Á., Agertz O., 2022, *MNRAS*, 516, 4922
- Rey M. P., Pontzen A., 2018, *MNRAS*, 474, 45
- Rey M. P., Pontzen A., Agertz O., Orkney M. D. A., Read J. I., Saintonge A., Pedersen C., 2019, *ApJ*, 886, L3
- Rey M. P., Pontzen A., Agertz O., Orkney M. D., Read J. I., Rosdahl J., 2020, *MNRAS*, 497, 1508
- Roth N., Pontzen A., Peiris H. V., 2016, *MNRAS*, 455, 974
- Sánchez-Janssen R. et al., 2019, *ApJ*, 878, 18
- Sand D. J. et al., 2022, *ApJ*, 935, L17
- Schmidt M., 1959, *ApJ*, 129, 243
- Seth A. C., Dalcanton J. J., Hodge P. W., Debattista V. P., 2006, *ApJ*, 132, 2539
- Seth A., Agüeros M., Lee D., Basu-Zych A., 2008a, *ApJ*, 678, 116
- Seth A. C., Blum R. D., Bastian N., Caldwell N., Debattista V. P., 2008b, *ApJ*, 687, 997
- Shlosman I., Begelman M. C., Frank J., 1990, *Nature*, 345, 679
- Siegel M. H. et al., 2007, *ApJ*, 667, L57
- Simon J. D., 2019, *ARA&A*, 57, 375
- Smith M. C., Bryan G. L., Somerville R. S., Hu C.-Y., Teyssier R., Burkhardt B., Hernquist L., 2021, *MNRAS*, 506, 3882
- Spengler C. et al., 2017, *ApJ*, 849, 55
- Springel V., di Matteo T., Hernquist L., 2005, *MNRAS*, 361, 776
- Stinson G., Seth A., Katz N., Wadsley J., Governato F., Quinn T., 2006, *MNRAS*, 373, 1074
- Stopyra S., Pontzen A., Peiris H., Roth N., Rey M. P., 2021, *ApJS*, 252, 28
- Taiolo M., Di Criscienzo M., D'Antona F., Caloi V., Ventura P., 2016, *MNRAS*, 457, 4525
- Teyssier R., 2002, *A&A*, 385, 337
- Thob A. C. R., Sanderson R. E., Eden A. P., Nikakhtar F., Panithanpaisal N., Garavito-Camargo N., Sharma S., 2023, *J. Open Source Software*, 9, 6234
- Tremaine S. D., Ostriker J. P., Spitzer L. J., 1975, *ApJ*, 196, 407
- Tsatsi A., Mastrobuono-Battisti A., van de Ven G., Perets H. B., Bianchini P., Neumayer N., 2017, *MNRAS*, 464, 3720
- Turner M. L., Côté P., Ferrarese L., Jordán A., Blakeslee J. P., Mei S., Peng E. W., West M. J., 2012, *ApJS*, 203, 5
- van Donkelaar F., Mayer L., Capelo P. R., Tamfal T., Quinn T. R., Madau P., 2024, *MNRAS*, 529, 4104
- van de Ven G., van den Bosch R. C. E., Verolme E. K., de Zeeuw P. T., 2006, *A&A*, 445, 513
- Walcher C.-J., Boeker T., Charlot S., Ho L. C., Rix H.-W., Rossa J., Shields J. C., van der Marel R. P., 2006, *ApJ*, 649, 692
- Woolsey S. E., Weaver T. A., 1995, *ApJS*, 101, 181
- Zocchi A., Gieles M., Hénault-Brunet V., 2019, *MNRAS*, 482, 4713

This paper has been typeset from a $\text{\TeX}/\text{\LaTeX}$ file prepared by the author.